J. Applied Membrane Science & Technology, Vol. 30, August 2026, 151-179

Selective Hydrogen Permeation and Transport Behaviour in Ruthenium-Impregnated Alumina Ceramic Membranes

Muktar M. Ramalan[1], Idris Hashim[1], Muhammad Dauda[2]

[1]Centre for Process and Membrane Technology, Robert Gordon University, Aberdeen, United Kingdom
[2]Department of Mechanical Engineering, Ahmadu Bello University, Zaria, Nigeria

Submitted: 13/06/2026. Revised edition: 14/07/2026. Accepted: 22/07/2026. Available online: 21/08/2026

ABSTRACT

Hydrogen and multi-gas permeation through ruthenium-impregnated alumina tubular membranes with nominal pore sizes of 15 nm and 6000 nm was investigated under non-reactive conditions at 100 °C and transmembrane pressure differences of 20–300 kPa. Single-gas permeation experiments using H_2, He, N_2, CO_2, and air were conducted to evaluate the influence of pore architecture and ruthenium incorporation on gas transport behaviour. For the 6000 nm membrane, the hydrogen flow rate increased from 1.09 to 8.39 L min^{-1}, whereas the 15 nm membrane exhibited hydrogen flow rates ranging from 0.97 to 4.61 L min^{-1} over the same pressure range. Despite the 400-fold difference in nominal pore size, the larger-pore membrane exhibited only a modest increase in hydrogen permeation, indicating that gas transport was governed by the overall membrane architecture rather than nominal pore diameter alone. This experimentally observed deviation from ideal pore-size scaling highlights the important influence of pore connectivity, tortuosity, support-layer resistance, and effective transport pathways in asymmetric ceramic membranes. Knudsen number analysis showed that the 6000 nm membrane operated predominantly within the viscous-flow regime, whereas the 15 nm membrane exhibited transitional Knudsen–viscous transport with enhanced molecular discrimination. SEM, EDX, contact-angle measurements, and gravimetric catalyst-loading analysis confirmed successful ruthenium incorporation without severe pore blockage or structural degradation. The results demonstrate that membrane architecture and Ru-induced surface modification exert a greater influence on gas permeation behaviour than nominal pore size alone under the non-reactive operating conditions investigated. These findings provide new insight into structure–transport relationships in Ru-modified ceramic membranes and offer guidance for the design of hydrogen-selective ceramic membrane systems.

Keywords: Hydrogen permeation; Ceramic membranes; Ruthenium impregnation; Gas transport; Knudsen diffusion; Membrane architecture

1.0 INTRODUCTION

Hydrogen is widely regarded as a promising energy carrier for low-carbon energy systems because of its high gravimetric energy density and environmentally benign

* Corresponding to: Muktar M. Ramalan (email: muktarmramalan@gmail.com)
DOI: https://doi.org/10.11113/jamst.v30n2.350

combustion products, producing primarily water [1–3]. The growing demand for clean energy technologies has increased interest in efficient hydrogen production, purification, and separation processes, particularly for hydrogen-rich gas streams generated from reforming, gasification, and related industrial processes [4–6].

Conventional hydrogen separation methods, including pressure swing adsorption and cryogenic distillation, are often associated with high energy consumption, complex operation, and significant capital costs [7, 8]. Membrane-based gas separation has therefore emerged as an attractive alternative due to its lower energy requirements, operational simplicity, and potential for continuous processing. Among available membrane materials, porous ceramic membranes have attracted considerable attention because of their excellent thermal stability, mechanical strength, and chemical resistance under harsh operating conditions [9].

Among ceramic materials, α-alumina (α-Al_2O_3) membranes are widely employed as robust supports for gas separation applications because of their well-defined pore structures, controllable morphology, and excellent thermal stability [10]. Ruthenium (Ru) was selected as the membrane modifier because of its high thermal stability, excellent catalytic activity towards hydrogen-related reactions, strong metal support interactions with alumina, and its ability to modify membrane surface physicochemical properties without significantly compromising the porous structure [11]. Although Ru has been widely employed in catalytic membrane reactors and heterogeneous catalysis, its influence on the intrinsic gas transport behaviour of porous ceramic membranes under non-reactive permeation conditions remains comparatively underexplored [12].

Recent studies have demonstrated that surface modification of ceramic membranes using metallic or catalytic phases can influence gas permeation by altering pore accessibility, surface energy, adsorption characteristics, and transport resistance. Ruthenium, palladium, nickel, and other transition metals have been investigated for hydrogen-related membrane applications because of their catalytic activity and favourable interactions with hydrogen species. However, most published studies have focused either on catalytic membrane reactors involving simultaneous reaction and separation or on dense metallic membranes operating via solution–diffusion mechanisms. Consequently, comparatively few studies have systematically investigated the intrinsic gas transport behaviour of Ru-modified porous ceramic membranes under non-reactive conditions, where the individual effects of membrane architecture and surface modification can be isolated and evaluated [11, 12].

Gas transport in porous ceramic membranes is generally governed by a combination of viscous (Poiseuille) flow and Knudsen diffusion, depending on pore size and operating conditions. Macroporous membranes are typically dominated by viscous flow, whereas mesoporous membranes often operate within a transitional regime in which both transport mechanisms contribute simultaneously [13]. As the pore diameter decreases, gas–wall interactions become increasingly important, resulting in a greater contribution from molecular diffusion mechanisms. Figure 1 illustrates the dominant transport mechanisms expected in ruthenium-impregnated α-alumina membranes with different pore structures, highlighting the predominance of viscous flow in the 6000 nm membrane and mixed Knudsen–viscous transport in the 15 nm membrane.

* Corresponding to: Muktar M. Ramalan (email: muktarmramalan@gmail.com)
DOI: https://doi.org/10.11113/jamst.v30n2.350

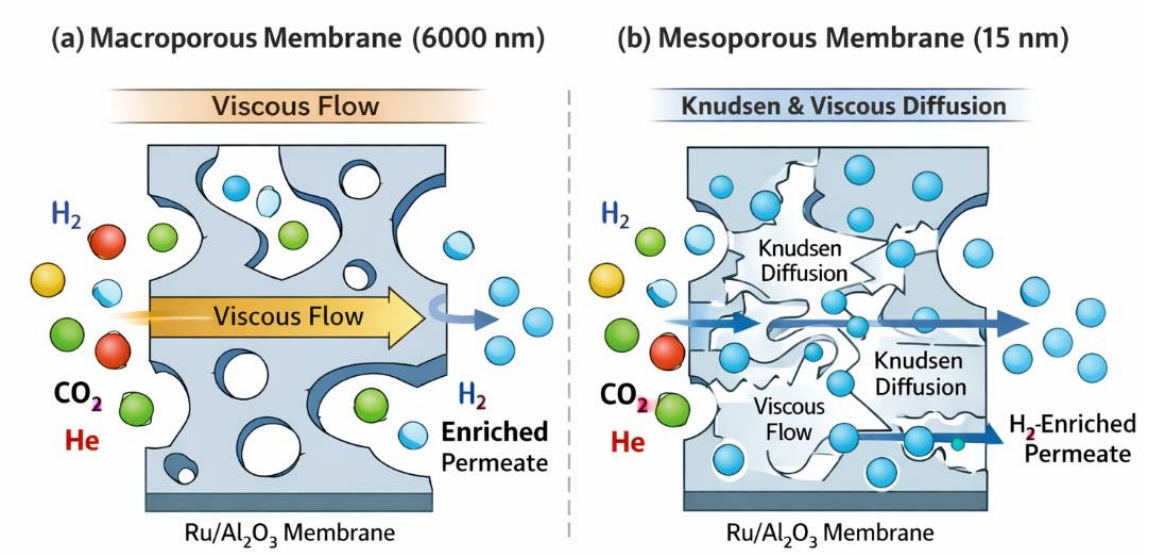

Figure 1. Schematic representation of gas transport mechanisms in ruthenium-impregnated α-alumina membranes: (a) viscous flow in macroporous (6000 nm) structures and (b) combined Knudsen–viscous transport in mesoporous (15 nm) membranes

Unlike catalytic membrane reactor studies involving simultaneous reaction and separation, the present work focuses specifically on non-reactive gas permeation in Ru-impregnated ceramic membranes. This approach enables the influence of pore architecture, ruthenium incorporation, and surface modification on intrinsic gas transport behaviour to be investigated independently of catalytic reaction effects under well controlled operating conditions [14].

Although viscous and Knudsen transport mechanisms are well established theoretically [12], their application to practical multilayer ceramic membranes frequently deviates from ideal transport predictions because gas permeation is governed by coupled structural factors, including pore connectivity, tortuosity, support-layer resistance, pore-size distribution, and gas–surface interactions. Consequently, membrane performance cannot always be predicted solely from nominal pore diameter. Furthermore, relatively few studies have directly compared Ru-impregnated mesoporous and macroporous ceramic membranes under identical non-reactive operating conditions [15]. As a result, the relative contributions of nominal pore size, membrane architecture, and ruthenium-induced surface modification to hydrogen and multi-gas transport behaviour remain insufficiently understood [16–18].

Understanding these non-ideal transport effects is important for the design and optimisation of hydrogen-selective ceramic membrane systems. In particular, identifying the relative contributions of pore size and membrane architecture is essential for improving membrane performance in hydrogen separation applications [19, 20].

This study therefore investigates hydrogen and multi-gas permeation through ruthenium-impregnated α-alumina membranes with nominal pore sizes of 15 nm and 6000 nm under identical operating conditions. The work focuses on: (i) evaluating gas transport behaviour across a transmembrane pressure difference range of 20–300 kPa; (ii) examining deviations from classical viscous and Knudsen transport predictions; (iii) assessing the influence of pore architecture and ruthenium impregnation on membrane

* Corresponding to: Muktar M. Ramalan (email: muktarmramalan@gmail.com)
DOI: https://doi.org/10.11113/jamst.v30n2.350

permeation behaviour; and (iv) determining whether practical membrane transport is governed primarily by nominal pore diameter or by the combined effects of membrane architecture and transport-pathway characteristics.

By combining gas permeation measurements with Knudsen number analysis, wettability measurements, catalyst loading evaluation, and SEM–EDX characterisation, this work provides an integrated experimental assessment of how membrane architecture and ruthenium-induced surface modification jointly influence gas transport behaviour under non-reactive conditions. Unlike previous studies that primarily emphasise catalytic membrane reactors or ideal transport models [21], the present work demonstrates experimentally that overall membrane architecture exerts a stronger influence on permeation behaviour than nominal pore diameter alone. These findings contribute to an improved understanding of structure–transport relationships relevant to the design and optimisation of hydrogen-selective ceramic membranes.

2.0 MATERIALS AND METHODS

This section describes the membrane materials, ruthenium impregnation procedure, thermal activation, gas permeation measurements, and characterisation methods used to evaluate gas transport behaviour through Ru-impregnated ceramic membranes.

2.1 Materials

Commercial asymmetric tubular ceramic membranes composed of alumina (Al_2O_3) and titania (TiO_2) were supplied by Ceramiques Techniques et Industrielles (CTI SA). The support composition was approximately 77 wt.% alumina and 23 wt.% titania. Two membranes with nominal pore sizes of 15 nm and 6000 nm were investigated.

The 6000 nm membrane had a total length of 446 mm, a permeable length of 378 mm, an outer diameter of 25 mm, and an inner diameter of 20 mm. The 15 nm membrane had a total length of 733 mm, a permeable length of 665 mm, and outer and inner diameters of 25 mm and 20 mm, respectively. Both membranes were supplied with glazed end sections for sealing during permeation experiments.

Ruthenium(III) chloride hydrate ($RuCl_3 \cdot xH_2O$, ≥99.9%, Sigma-Aldrich) was used as the catalyst precursor. Deionised water was used for membrane preparation and impregnation. Hydrogen (99.999%), helium (99.999%), nitrogen (99.999%), carbon dioxide (99.995%), and compressed dry air were supplied by BOC (UK) and used without further purification.

2.2 Membrane Preparation and Ruthenium Impregnation

Prior to catalyst impregnation, the ceramic membranes were thoroughly rinsed with deionised water to remove dust, residual manufacturing contaminants, and loosely adhered surface particles that could interfere with catalyst deposition. The cleaned membranes were dried in a convection oven at 65 °C for 24 h to eliminate residual moisture. After cooling to room temperature in a desiccator, each membrane was weighed using an analytical balance (±0.1 mg) to obtain the initial support mass required for subsequent catalyst-loading calculations. To prevent catalyst deposition within the membrane lumen,

* Corresponding to: Muktar M. Ramalan (email: muktarmramalan@gmail.com)
DOI: https://doi.org/10.11113/jamst.v30n2.350

both glazed ends were sealed with polytetrafluoroethylene (PTFE) tape, ensuring that impregnation was confined to the permeable membrane region.

Ruthenium was deposited using a single-cycle wet impregnation method. The precursor solution was prepared by dissolving 30.0 g of ruthenium(III) chloride hydrate ($RuCl_3 \cdot xH_2O$) in 100 mL of deionised water, corresponding to a concentration of approximately 300 g L^{-1}. Prior to impregnation, the membranes were immersed in deionised water for 2 h to ensure complete wetting of the pore network and facilitate penetration of the precursor solution into the accessible porous structure. The pre-wetted membranes were subsequently immersed in the ruthenium precursor solution for 24 h under static conditions at ambient temperature without external agitation, allowing Ru^{3+} ions to infiltrate the porous network through capillary action and molecular diffusion.

Following impregnation, the membranes were removed from the precursor solution, allowed to drain for approximately 10 min to remove excess solution from the external surface, and air-dried under ambient conditions for 24 h. The membranes were then dried in a convection oven at 65 °C for 6 h prior to thermal treatment. This controlled drying procedure minimised rapid solvent evaporation during subsequent calcination and promoted stable deposition of the ruthenium precursor within the membrane pores.

The amount of deposited ruthenium was determined gravimetrically from the difference between the membrane mass before and after impregnation according to:
Catalyst loading following ruthenium impregnation was determined gravimetrically using Equation (8):

$$Loading\ (\%) = \frac{W_3}{W_2} \times 100 \quad (1)$$

where W_1 is the initial support mass, W_2 is the final membrane mass after ruthenium impregnation and thermal treatment, and W_3 ($=W_2 - W_1$) represents the mass of ruthenium deposited within the membrane structure.

The gravimetric analysis indicated ruthenium loadings of approximately 0.08 wt.% for the 15 nm membrane and 0.33 wt.% for the 6000 nm membrane, demonstrating greater Ru uptake by the larger-pore membrane because of its higher accessible pore volume during the impregnation process.

2.3 Calcination and Reduction

After drying, the membranes were calcined in air at 400 °C for 4 h using a heating rate of 5 °C min^{-1}. The furnace was then allowed to cool naturally to room temperature.
Prior to permeation testing, the calcined membranes were reduced in a stainless-steel tubular reactor. The system was first purged with nitrogen at 100 mL min^{-1} for 30 min to remove residual air. The temperature was increased to 300 °C at a heating rate of 5 °C min^{-1}, after which hydrogen was introduced at 100 mL min^{-1} for 30 min to reduce ruthenium oxide species according to:

$$RuO_2 + 2H_2 \rightarrow Ru + 2H_2O$$

* Corresponding to: Muktar M. Ramalan (email: muktarmramalan@gmail.com)
DOI: https://doi.org/10.11113/jamst.v30n2.350

Following reduction, helium was passed through the system for 30 min before cooling to the permeation test temperature of 100 °C.

2.4 Gas Permeation Setup

Single-gas permeation experiments were conducted using a custom-built tubular membrane permeation system comprising high-purity gas cylinders, pressure regulators, mass flow controllers, pressure gauges, a stainless-steel membrane module, an electrically heated chamber with proportional-integral-derivative (PID) temperature control, and a calibrated volumetric flow meter. A schematic of the complete experimental arrangement is presented in Figure 2.

As shown in Figure 2, the feed gas was introduced through the lumen side of the tubular membrane, while the permeate was collected from the shell side. Feed pressure was regulated using a precision pressure regulator, whereas the permeate side was maintained at approximately atmospheric pressure throughout the experiments. The membrane module temperature was maintained at 100 °**C** using a PID-controlled heating system. Permeation measurements were performed over transmembrane pressure differences ranging from 20 to 300 kPa. Gas flow rates were recorded after steady-state conditions had been established at each pressure level to ensure reproducible evaluation of pressure dependent permeation behaviour.

Figure 2. Experimental setup showing the gas permeation apparatus, including the pressure gauge (1), membrane module wrapped with heating tape (2), gas regulator (3), gas cylinder (4), temperature controller (5), volumetric flow meter (6), and temperature indicator (7).

2.5 Permeation Measurement Procedure

Hydrogen, helium, nitrogen, carbon dioxide, and dry air were tested individually under non-reactive permeation conditions. Prior to each experiment, the system was purged with the test gas for 10 min to ensure steady-state composition within the membrane module. Permeation measurements were conducted over transmembrane pressure differences

* Corresponding to: Muktar M. Ramalan (email: muktarmramalan@gmail.com)
DOI: https://doi.org/10.11113/jamst.v30n2.350

ranging from 20 to 300 kPa. At each pressure step, the system was stabilised for approximately 3–5 min before flow measurements were recorded. Three replicate measurements were obtained for each condition and averaged.

Gas permeability was calculated using:

$$P = \frac{QL}{A\Delta P} \tag{2}$$

where Q is the measured volumetric gas flow rate ($m^3\ s^{-1}$), L is the effective thickness of the membrane layer through which gas permeation occurred, A is the effective permeation area corresponding to the exposed cylindrical membrane surface available for gas transport (excluding the glazed sealing sections), and ΔP is the transmembrane pressure difference. The effective membrane area was calculated from the permeable length and external diameter of each tubular membrane, while the membrane thickness corresponded to the active porous membrane wall supplied by the manufacturer. This expression is consistent with conventional membrane permeation analysis reported in the literature [22]. Ideal selectivity was determined from:

$$\propto_{A/B} = \frac{P_A}{P_B} \tag{3}$$

where P_a and P_β are the permeabilities of gases A and B, respectively. The ideal selectivity represents the permeability ratio obtained from individual single-gas permeation measurements and provides an indication of the membrane's intrinsic gas discrimination in the absence of competitive adsorption or multicomponent diffusion effects [22].

2.6 Contact Angle Measurement

Surface wettability was evaluated using dynamic contact angle measurements to investigate the effects of pore structure and ruthenium impregnation on membrane surface behaviour. Water droplets (5 μL) were deposited onto the membrane surfaces and monitored as a function of time to evaluate droplet spreading and wetting characteristics. The droplet volume was selected to minimise curvature effects associated with the tubular membrane geometry. Wettability behaviour was interpreted qualitatively using the Young–Wenzel and Cassie–Baxter wetting models [23, 24].
The Young–Wenzel relationship is expressed as

$$Cos\ \theta_w = r\ cos\ \theta_\gamma \tag{4}$$

where:

θ_W is the apparent contact angle on the rough surface,

θ_Y is the intrinsic Young contact angle,

r is the surface roughness factor.

The Cassie–Baxter relationship is given by [24]

* Corresponding to: Muktar M. Ramalan (email: muktarmramalan@gmail.com)
DOI: https://doi.org/10.11113/jamst.v30n2.350

$$cos\theta_{CB} = f_s(cos\theta_y + 1) - 1 \quad (5)$$

where:

θ_{CB} is the apparent Cassie–Baxter contact angle,

f_s is the solid–liquid contact fraction,

θ_Y is the intrinsic Young contact angle.

These models were used to assist in the qualitative interpretation of the wettability behaviour observed for the Ru-modified ceramic membranes.

2.7 Transport Regime Analysis

Gas transport behaviour was interpreted using the Knudsen number:

$$Kn = \frac{\lambda}{d_p} \quad (6)$$

where λ is the molecular mean free path and d_p is the nominal membrane pore diameter. The molecular mean free path was estimated from standard kinetic gas theory as a function of gas temperature and pressure using published gas kinetic relationships. Because the mean free path is inversely proportional to gas pressure, increasing operating pressure reduces λ and consequently decreases the Knudsen number. The calculated values therefore provide an estimate of the dominant gas transport regime under the experimental operating conditions.

For $Kn \ll 0.01$, viscous flow dominates; for $Kn \gg 1$, Knudsen diffusion dominates; and for $0.01 < Kn < 1$, transitional transport is expected [25, 26].

Under the present experimental conditions, the 6000 nm membrane was expected to operate predominantly within the viscous-flow regime, whereas the 15 nm membrane was expected to exhibit mixed Knudsen–viscous transport behaviour.

The transport regime analysis was used to interpret the relative contributions of viscous flow and Knudsen diffusion to gas permeation behaviour in the membranes. Comparison between theoretical transport expectations and experimentally measured permeation behaviour enabled assessment of the influence of pore architecture and ruthenium impregnation on gas transport characteristics.

2.7 Surface and Structural Characterisation

Surface wettability of the membranes was evaluated using an optical tensiometer (OneAttension ThetaLite, Biolin Scientific). Approximately 5 µL deionised water droplets were deposited onto the membrane surface at ambient conditions, and static contact angles were determined using image analysis software integrated with the instrument. Measurements were performed at three different surface locations for each membrane sample, and the reported values represent the average of three independent measurements to ensure reproducibility.

* Corresponding to: Muktar M. Ramalan (email: muktarmramalan@gmail.com)
DOI: https://doi.org/10.11113/jamst.v30n2.350

The droplet volume was selected to minimise gravitational distortion and maintain stable droplet geometry during measurement. Although the membranes possessed a curved tubular geometry, the droplet diameter remained sufficiently small relative to the membrane curvature, such that curvature effects on contact angle determination were considered negligible.

Surface morphology, microstructural features, and elemental composition of the membranes were characterised using scanning electron microscopy (SEM) coupled with energy-dispersive X-ray spectroscopy (EDX). Prior to imaging, membrane samples were mounted on conductive carbon stubs and sputter-coated with a thin gold layer to minimise surface charging during electron beam exposure.

SEM analysis was performed using an accelerating voltage of 20 kV, working distance of approximately 8.5 mm, and probe current of 350 pA. Representative micrographs were obtained at multiple magnifications to examine surface morphology, pore architecture, and structural integrity following ruthenium impregnation and thermal treatment. SEM observations were used for comparative morphological assessment rather than evaluation of catalyst distribution. The SEM observations were used primarily for comparative morphological assessment rather than direct nanoscale pore-size quantification.

EDX point analysis was performed simultaneously with SEM imaging to verify the presence of ruthenium together with the major support elements (aluminium, titanium, and oxygen) on the membrane surface. The EDX analysis provided qualitative confirmation of catalyst incorporation following the impregnation and thermal treatment processes. However, elemental mapping of ruthenium distribution was not performed; therefore, the EDX results were used only to confirm elemental composition and the presence of Ru rather than to evaluate its spatial dispersion within the membrane structure [27].

3.0 RESULTS AND DISCUSSION

The results presented in this section focus on the influence of ruthenium impregnation and membrane pore architecture on non-reactive gas permeation behaviour in asymmetric alumina ceramic membranes. Structural characterisation, surface analysis, and single-gas permeation experiments were performed to evaluate the relationship between membrane morphology, surface modification, and pressure-driven gas transport under controlled operating conditions. Particular attention was given to the influence of pore architecture on permeation behaviour and gas transport mechanisms.

3.1 Membrane Characterisation

The ruthenium-impregnated ceramic membranes were characterised using scanning electron microscopy (SEM), energy-dispersive X-ray spectroscopy (EDX), contact angle measurements, and single-gas permeation analysis to establish relationships between membrane structure, surface modification, and gas transport behaviour.

SEM observations indicated that both membranes retained their asymmetric porous structures following ruthenium impregnation, calcination, and reduction treatment. No obvious macroscopic structural defects, such as cracking, delamination, or structural collapse, were observed after thermal processing. The membrane with a nominal pore size of 6000 nm exhibited an open macroporous support structure with interconnected flow

* Corresponding to: Muktar M. Ramalan (email: muktarmramalan@gmail.com)
DOI: https://doi.org/10.11113/jamst.v30n2.350

channels favourable for pressure-driven bulk gas transport. In contrast, the 15 nm membrane exhibited a denser selective surface layer supported by a more porous substructure, consistent with asymmetric ceramic membrane architectures commonly employed for selective gas transport applications [28].

Although the SEM magnifications employed were not sufficient to directly resolve individual 15 nm pores, the observed surface morphology remained consistent with the nominal membrane characteristics specified by the manufacturer. Accordingly, the SEM observations were used primarily to assess overall structural integrity and comparative morphology rather than to quantify pore dimensions or determine the extent of pore blockage following ruthenium impregnation. The approximately linear gas permeation behaviour observed over the investigated pressure range nevertheless indicates that the accessible transport pathways remained functional after membrane modification.

EDX spectra confirmed the presence of ruthenium together with aluminium, titanium, and oxygen, demonstrating successful incorporation of Ru into both membrane structures. Because elemental mapping was not performed, the spatial distribution of ruthenium across the membrane surface could not be assessed directly. Nevertheless, the detected Ru peaks, together with the gravimetric catalyst loading measurements presented in Section 3.6, provide complementary evidence that catalyst incorporation was successfully achieved. Therefore, the EDX analysis confirms the presence of ruthenium but does not permit conclusions regarding the uniformity of catalyst distribution.

Contact angle measurements revealed moderate changes in surface wettability following ruthenium treatment, indicating alteration of membrane surface properties by the deposited metal species. These changes may influence gas–surface interactions, adsorption behaviour, and local transport characteristics, particularly for CO_2, which exhibits relatively stronger surface affinity than the other gases investigated.

Overall, the characterisation results confirm successful ruthenium incorporation while preserving the macroscopic integrity of both membrane architectures. Although higher-resolution SEM imaging and EDX elemental mapping would provide a more detailed assessment of catalyst dispersion and local pore coverage, the combined SEM observations, EDX spectra, gravimetric catalyst loading measurements, and permeation results consistently indicate that Ru impregnation did not significantly impede the accessible gas transport pathways responsible for membrane permeation.

3.2 Single Gas Permeation Behaviour

Figures 3 and 4 present the permeation rates of H_2, He, N_2, air, and CO_2 through the ruthenium-impregnated 6000 nm and 15 nm alumina membranes, respectively, at 100 °C over transmembrane pressure differences ranging from 20 to 300 kPa.

* Corresponding to: Muktar M. Ramalan (email: muktarmramalan@gmail.com)
DOI: https://doi.org/10.11113/jamst.v30n2.350

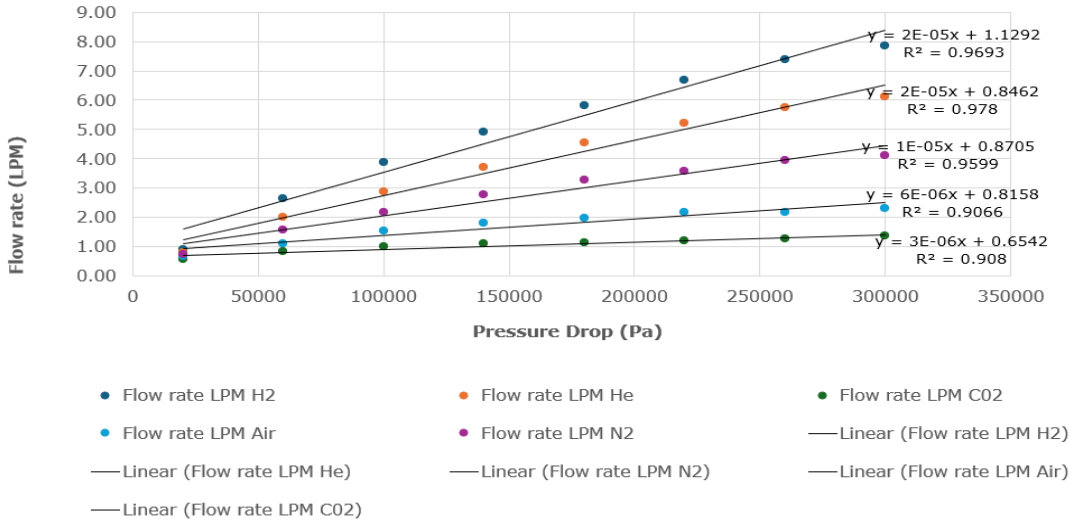

Figure 3. Single-gas permeation rates of H_2, He, N_2, air, and CO_2 through ruthenium-impregnated alumina membrane with 6000 nm nominal pore size at 100 °C under transmembrane pressure differences of 20–300 kPa.

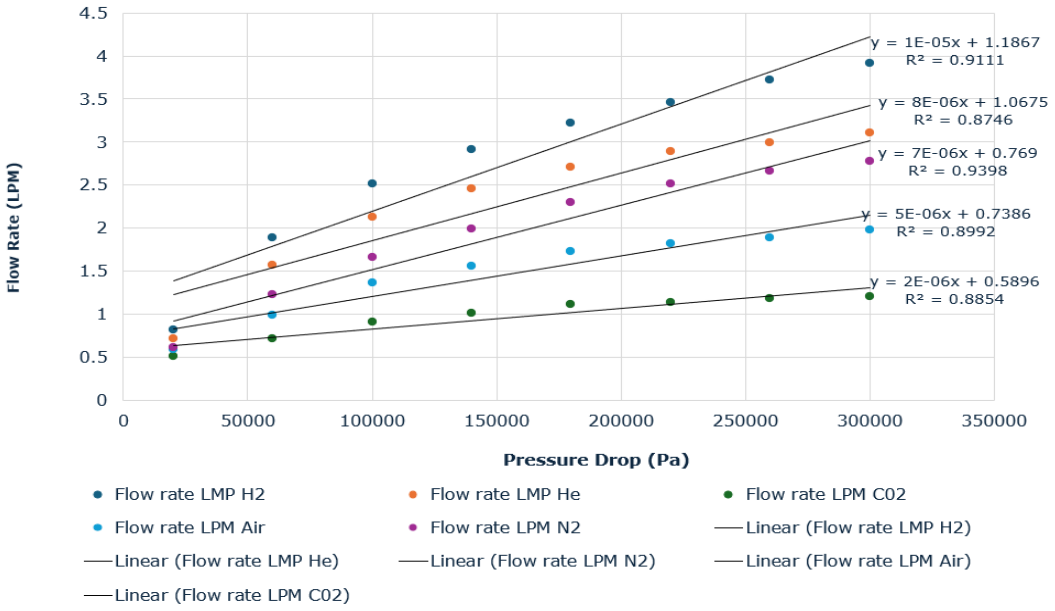

Figure 4. Single-gas permeation rates of H_2, He, N_2, air, and CO_2 through ruthenium-impregnated alumina membrane with 15 nm nominal pore size at 100 °C under transmembrane pressure differences of 20–300 kPa

For both membranes, permeation rates increased approximately linearly with increasing transmembrane pressure difference, indicating that pressure-driven transport was the dominant permeation mechanism over the investigated operating range. The observed linear behaviour is consistent with combined viscous and molecular transport mechanisms commonly encountered in porous ceramic membranes, where gas flux increases proportionally with the applied pressure gradient [29].

* Corresponding to: Muktar M. Ramalan (email: muktarmramalan@gmail.com)
DOI: https://doi.org/10.11113/jamst.v30n2.350

For the 6000 nm membrane, hydrogen permeation increased from 1.09 to 8.39 L min^{-1} as the transmembrane pressure increased from 20 to 300 kPa. Over the same pressure range, helium permeation increased from 0.98 to 7.61 L min^{-1}, nitrogen from 0.91 to 6.52 L min^{-1}, and carbon dioxide from 0.62 to 2.27 L min^{-1}. The relatively high permeation rates and similar pressure-dependent trends for the different gases indicate that viscous (Poiseuille-type) flow was the dominant transport mechanism within the macroporous membrane, where gas transport is governed primarily by the applied pressure gradient, pore accessibility, and gas viscosity. The consistently higher hydrogen permeation suggests that the Ru impregnation procedure preserved the accessible gas transport pathways while modifying the membrane surface, thereby maintaining favourable hydrogen transport characteristics.

In contrast, the 15 nm membrane exhibited lower permeation rates for all gases. Hydrogen permeation increased from 0.97 to 4.61 L min^{-1}, nitrogen from 0.68 to 2.74 L min^{-1}, and carbon dioxide from 0.51 to 1.64 L min^{-1} over the same pressure range. Although permeation increased linearly with pressure, greater separation between lighter and heavier gases was observed compared with the 6000 nm membrane. The enhanced molecular discrimination suggests that the smaller effective pore size reduced the contribution of bulk viscous flow while increasing the relative importance of Knudsen diffusion and transitional transport mechanisms [12, 30, 31]. Under these conditions, gas transport becomes increasingly dependent on molecular weight, kinetic diameter, and gas–wall interactions, resulting in improved hydrogen-selective permeation relative to the heavier gases.

A notable observation is that the 6000 nm membrane did not exhibit the extremely large increase in permeation that would be expected from ideal pore-radius scaling alone. Classical viscous-flow theory predicts that gas flux should increase strongly with increasing pore diameter; however, the experimentally observed difference in permeation between the two membranes was considerably smaller than that predicted by the idealised Poiseuille relationship.

This behaviour indicates that nominal pore diameter was not the sole parameter governing overall membrane transport resistance. Instead, additional structural characteristics, including membrane thickness, pore connectivity, tortuosity, effective porosity, entrance and exit losses, and support-layer resistance, contributed significantly to the observed permeation behaviour [32]. In particular, the asymmetric architecture of the 15 nm membrane may have reduced effective transport resistance through interconnected transport pathways despite its much smaller nominal pore diameter.

Comparison of the individual gases further illustrates the influence of molecular properties on membrane transport. Hydrogen consistently exhibited the highest permeation rates owing to its low molecular weight, high molecular velocity, and small kinetic diameter, which favour rapid transport through porous membranes. Helium, despite its lower molecular weight, exhibited slightly lower permeation than hydrogen, reflecting differences in gas–surface interactions and transport behaviour within the Ru-modified membrane. Nitrogen and air exhibited comparable permeation rates because air consists predominantly of nitrogen (approximately 78 vol.%), causing its transport behaviour to closely resemble that of nitrogen under the present non-reactive conditions. Carbon dioxide consistently exhibited the lowest permeation despite its relatively small kinetic diameter. This behaviour is attributed to its higher molecular weight together with stronger

* Corresponding to: Muktar M. Ramalan (email: muktarmramalan@gmail.com)
DOI: https://doi.org/10.11113/jamst.v30n2.350

adsorption and gas–surface interactions within the Ru-modified membrane pores, which reduce its effective transport rate.

These results demonstrate that gas permeation is governed by the combined effects of pore architecture, membrane structure, and transport regime rather than by nominal pore diameter alone. The findings further indicate that controlled ruthenium impregnation modified the membrane surface without compromising accessible transport pathways, thereby preserving favourable hydrogen permeation while maintaining the structural characteristics responsible for gas transport.

3.3 Knudsen Number Analysis

For the 15 nm membrane, the Knudsen number decreased from 13.3 at 20 kPa to 0.67 at 300 kPa, reflecting a gradual transition from Knudsen-dominated transport towards mixed Knudsen–viscous flow with increasing pressure. By contrast, the 6000 nm membrane exhibited Knudsen numbers below 0.01 over most of the investigated pressure range, confirming that viscous flow was the dominant transport mechanism. These theoretical predictions are consistent with the experimentally observed permeation behaviour, in which the 15 nm membrane exhibited enhanced molecular discrimination, whereas the 6000 nm membrane displayed higher pressure-driven permeation rates. The calculated Knudsen numbers, corresponding flow regimes, and estimated molecular mean free paths for hydrogen at different operating pressures are summarised in Table 1.

Table 1. Estimated Knudsen Number for Hydrogen at 100 °C

Pressure (kPa)	Mean Free Path λ (μm)	Kn (15 nm)	Kn (6000 nm)	Flow Regime (15 nm)	Flow Regime (6000 nm)
20	0.20	13.3	0.033	Knudsen/Transition	Slip/Viscous
50	0.08	5.3	0.013	Transition	Slip
100	0.04	2.7	0.0067	Transition	Viscous
200	0.02	1.3	0.0033	Transition	Viscous
300	0.01	0.67	0.0017	Transition	Viscous

The calculated Knudsen numbers support the experimentally observed gas transport behaviour. The 15 nm membrane operated predominantly within the transitional flow regime, where both Knudsen diffusion and viscous flow contributed to gas transport. Consequently, the membrane exhibited lower permeation rates but improved molecular discrimination owing to the greater influence of gas–wall interactions within the smaller pore structure.

By comparison, transport through the 6000 nm membrane was governed predominantly by viscous flow, where bulk gas movement through the macroporous structure produced substantially higher permeation rates with lower selectivity characteristics [31-33].

Figure 5 illustrates the variation of Knudsen number with operating pressure for hydrogen permeation through both membrane structures. In both cases, the Knudsen number decreased with increasing pressure as a consequence of reduced molecular mean

* Corresponding to: Muktar M. Ramalan (email: muktarmramalan@gmail.com)
DOI: https://doi.org/10.11113/jamst.v30n2.350

free path at higher gas density. The clear separation between the two membrane behaviours demonstrates the strong influence of pore architecture on gas transport regime under otherwise identical operating conditions [34].

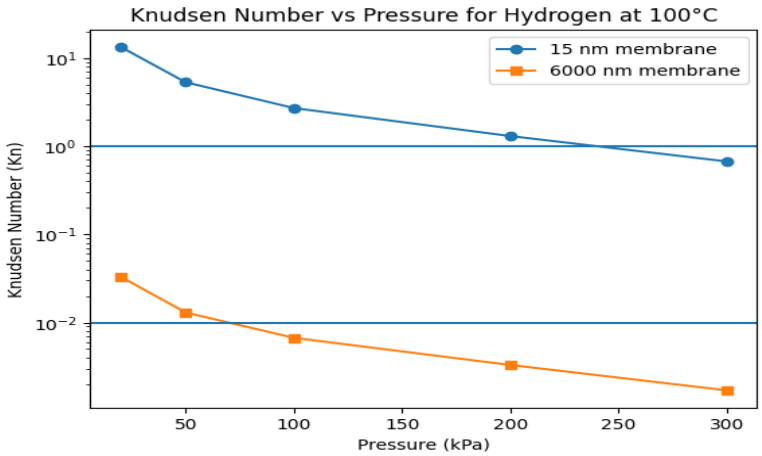

Figure 5. Variation of Knudsen number with operating pressure for hydrogen permeation through the 15 nm and 6000 nm ceramic membranes at 100 °C

3.4 Comparison with Ideal Viscous Flow Predictions

To assess the extent to which the experimental permeation behaviour followed classical viscous-flow theory, the hydrogen permeation data were compared with predictions based on the classical Poiseuille relationship, which was used as a theoretical benchmark for ideal cylindrical capillaries [35].

$$Q \propto r^4 \tag{7}$$

where Q is the volumetric flow rate and r is the pore radius. This relationship predicts a strong dependence of permeation on pore size.

The membranes investigated in this study possessed nominal pore diameters of 15 nm and 6000 nm, corresponding to a pore-size ratio of 400. Applying the classical Poiseuille relationship to these nominal pore diameters yields a theoretical permeation ratio of:

$$\frac{6000}{15} = 400 \tag{8}$$

For an ideal capillary system described by Poiseuille flow, the theoretical permeation ratio may be estimated as:

$$400^4 = 2.56 \times 10^{10} \left(\frac{6000}{15}\right)^4 \tag{9}$$

Thus, classical viscous flow theory predicts that the 6000 nm membrane should exhibit a permeation rate approximately (2.56 x 10^{10}) times greater than that of the 15 nm membrane.

* Corresponding to: Muktar M. Ramalan (email: muktarmramalan@gmail.com)
DOI: https://doi.org/10.11113/jamst.v30n2.350

The experimental results differed substantially from this prediction. At a transmembrane pressure difference of 300 kPa, hydrogen permeation was 8.39 L min^{-1} for the 6000 nm membrane and 4.61 L min^{-1} for the 15 nm membrane, corresponding to an experimental permeation ratio of only 1.82. Similar behaviour was observed at lower pressures, where the measured permeation rates differed by less than a factor of two.

A comparison between the theoretical permeation ratio predicted by classical Poiseuille flow and the experimentally measured hydrogen permeation behaviour is presented in Table 2. The results highlight the large discrepancy between ideal pore-radius scaling predictions and the observed transport behaviour of the multilayer ceramic membranes investigated in this study.

Table 2. Comparison between theoretical viscous flow prediction and experimental hydrogen permeation behaviour

Parameter	**15 nm Membrane**	**6000 nm Membrane**
Nominal pore size (nm)	15	6000
Hydrogen flow rate at 300 kPa (L min^{-1})	4.61	8.39
Experimental permeation ratio	1.00	1.82
Theoretical Poiseuille ratio	1.00	2.56×10^{10}

The substantial difference between theoretical and experimental permeation ratios demonstrates that nominal pore diameter alone does not govern gas transport behaviour in the investigated ceramic membranes. The Poiseuille model assumes straight cylindrical capillaries of uniform radius and negligible structural resistance. In contrast, the membranes examined in this study possess asymmetric multilayer architectures comprising interconnected pore networks, tortuous flow pathways, support structures, and non-uniform pore geometries.

Consequently, gas transport is influenced by the combined resistance of the entire membrane structure rather than by nominal surface pore diameter alone. Factors including pore connectivity, tortuosity, support-layer resistance, pore-size distribution, and effective transport pathways all contribute to the overall permeation behaviour. Similar deviations from ideal pore-size scaling have been reported for multilayer ceramic membranes, where permeability frequently exhibits a weaker dependence on nominal pore diameter than predicted by simplified capillary flow models [36, 37].

Although the two membranes differed by a factor of 400 in nominal pore diameter, the experimentally observed hydrogen permeation rate increased by only approximately 1.8-fold. This result demonstrates that overall membrane architecture, including pore connectivity, tortuosity, support-layer resistance, and effective transport pathways, exerts a much greater influence on gas transport behaviour than nominal pore size alone under the investigated operating conditions.

* Corresponding to: Muktar M. Ramalan (email: muktarmramalan@gmail.com)
DOI: https://doi.org/10.11113/jamst.v30n2.350

3.5 Gas Transport Behaviour, Selectivity and Flow Resistance

The combined permeation, Knudsen-number, and theoretical flow analyses demonstrate that gas transport through the Ru-impregnated ceramic membranes was governed by the interaction between membrane architecture, transport regime, and gas molecular properties rather than by nominal pore diameter alone. While Sections 3.2–3.4 describe the individual permeation behaviour and transport mechanisms, the present section integrates these findings to explain the overall membrane performance.

The 6000 nm membrane consistently exhibited higher permeation rates than the 15 nm membrane for all gases investigated. Its very low Knudsen numbers confirmed that transport was dominated primarily by viscous (Poiseuille-type) flow, resulting in high gas throughput but relatively limited molecular discrimination. By contrast, the 15 nm membrane operated within the transitional Knudsen–viscous regime, where increased gas-wall interactions enhanced molecular discrimination while reducing overall permeance [31, 38].

For both membranes, the permeation sequence remained:

$H_2 > He > N_2 \approx Air > CO_2$

This trend reflects the combined influence of molecular weight, kinetic diameter, molecular velocity, and gas–surface interactions. Hydrogen exhibited the highest permeation because of its low molecular weight, high molecular velocity, and small kinetic diameter. Helium permeated slightly more slowly despite its lower molecular weight, indicating that transport was also influenced by interactions between the gas molecules and the Ru-modified membrane surface. Nitrogen and air exhibited similar permeation behaviour because air consists predominantly of nitrogen, whereas carbon dioxide consistently showed the lowest permeation, which is attributed to its higher molecular weight together with stronger adsorption and gas-surface interactions within the membrane pores [39].

The comparison between the two membrane architectures clearly illustrates the permeability–selectivity trade-off characteristic of porous ceramic membranes. At a transmembrane pressure difference of 300 kPa, hydrogen permeation through the 15 nm membrane reached approximately 4.61 L min^{-1} compared with 2.74 L min^{-1} for nitrogen and 1.64 L min^{-1} for carbon dioxide, demonstrating improved molecular discrimination. In contrast, the 6000 nm membrane exhibited smaller differences among the investigated gases because transport remained dominated by bulk viscous flow through the larger interconnected pore network [40].

Hydrogen selectivity was therefore evaluated using H_2/N_2 and H_2/CO_2 permeability ratios, as these gas pairs are directly relevant to hydrogen purification and carbon-containing process streams. H_2/He selectivity was not evaluated because both gases are light, weakly adsorbing molecules with similar transport behaviour, making helium primarily a reference gas rather than a practical separation target. Likewise, H_2/air selectivity was not determined because air is a multicomponent gas mixture rather than a single gas, and its permeation behaviour closely followed that of nitrogen under the present non-reactive conditions. At 300 kPa, the 15 nm membrane exhibited H_2/N_2 and H_2/CO_2

* Corresponding to: Muktar M. Ramalan (email: muktarmramalan@gmail.com)
DOI: https://doi.org/10.11113/jamst.v30n2.350

selectivity values of approximately 1.7 and 2.8, respectively, whereas the corresponding values for the 6000 nm membrane were approximately 1.3 and 3.7. The higher H_2/N_2 selectivity obtained for the 15 nm membrane is consistent with the greater contribution of Knudsen diffusion within the finer pore structure [41, 42].

The moderate selectivity values obtained are characteristic of porous ceramic membranes operating under non-reactive conditions, where gas transport is governed by viscous flow and Knudsen diffusion rather than molecular sieving. Consequently, hydrogen selectivity remains lower than that reported for dense palladium-based membranes but agrees well with values commonly reported for porous ceramic membrane systems [43–46]. Similar behaviour has also been reported for metal-modified porous ceramic membranes, where surface modification alters gas–surface interactions while the dominant transport mechanism remains controlled primarily by membrane pore architecture [47, 48].

The combined experimental evidence further demonstrates that the large difference in nominal pore diameter between the two membranes did not produce the extreme permeation difference predicted by ideal Poiseuille theory. Instead, the overall transport behaviour reflects the combined influence of pore connectivity, tortuosity, support-layer resistance, effective transport pathways, and membrane architecture [37, 49]. These observations reinforce the conclusion that practical gas transport in asymmetric ceramic membranes cannot be predicted from nominal pore diameter alone.

Ruthenium impregnation modified the membrane surface without fundamentally altering the governing transport mechanism. The SEM observations, EDX spectra, contact-angle measurements, catalyst-loading analysis, and permeation results collectively indicate that Ru incorporation altered the surface physicochemical properties and gas–surface interactions while preserving the accessible pore network responsible for gas transport. Accordingly, ruthenium acted primarily as a surface modifier rather than as a structural transport barrier. This behaviour provides a useful foundation for future investigations under reactive operating conditions, where the catalytic activity of ruthenium may contribute directly to hydrogen production and separation [49, 50].

The results demonstrate that gas transport in Ru-impregnated ceramic membranes is governed by the combined effects of membrane architecture, transport regime, gas molecular properties, and surface modification. While the 6000 nm membrane maximised permeance, the 15 nm membrane provided improved molecular discrimination, confirming that optimisation of pore architecture remains the primary design parameter for hydrogen-selective ceramic membranes.

3.6 Catalyst Loading and Ru Distribution

The catalyst loading values obtained for the 15 nm and 6000 nm membranes are presented in Table 3. Catalyst loading was determined gravimetrically using the procedure described in Section 2.2.

* Corresponding to: Muktar M. Ramalan (email: muktarmramalan@gmail.com)
DOI: https://doi.org/10.11113/jamst.v30n2.350

Table 3. Catalyst loading for 15 nm and 6000 nm membranes

Membrane pore size	**15 nm**	**6000 nm**
Fresh support W_1 (g)	483.5	268.8
Final mass W_2 (g)	483.9	269.7
Deposited Ru W_3 (g)	0.4	0.9
Loading (%)	0.08	0.33

The 6000 nm membrane exhibited a higher overall ruthenium loading than the 15 nm membrane. This difference is attributed primarily to the larger accessible pore volume and greater pore accessibility, which facilitated increased uptake of the Ru precursor during the impregnation process.

SEM–EDX analysis confirmed the presence of ruthenium on both membrane surfaces following impregnation and thermal treatment. However, as elemental mapping was not performed, the spatial distribution of Ru within the membrane structure cannot be determined from the present EDX analysis. Accordingly, the gravimetric loading values indicate differences in the total amount of deposited ruthenium but do not provide information regarding catalyst uniformity or dispersion.

The approximately linear increase in gas permeation with transmembrane pressure after impregnation indicates that ruthenium incorporation did not introduce significant transport limitations within the accessible pore network. Although the available SEM resolution does not permit direct assessment of nanoscale pore blockage, the permeation results suggest that the deposited Ru did not substantially obstruct the transport pathways responsible for gas flow.

The lower catalyst loading observed for the 15 nm membrane is consistent with its finer pore structure and lower accessible pore volume, whereas the larger pore architecture of the 6000 nm membrane facilitated greater precursor uptake during impregnation.

These results demonstrate that controlled ruthenium impregnation was successfully achieved in both membrane architectures while preserving the gas transport characteristics required for subsequent permeation measurements.

3.7 Structure Transport Relationship and Design Implications

The combined experimental and characterisation results demonstrate that membrane architecture is the primary factor governing gas transport behaviour in the Ru-impregnated ceramic membranes investigated in this study. Although ruthenium modified the membrane surface, the observed permeation behaviour remained controlled principally by pore architecture and the associated transport regime.

The 6000 nm membrane exhibited substantially higher permeation rates than the 15 nm membrane, consistent with transport dominated by viscous (Poiseuille-type) flow through its interconnected macroporous structure. The larger pore channels facilitated greater

* Corresponding to: Muktar M. Ramalan (email: muktarmramalan@gmail.com)
DOI: https://doi.org/10.11113/jamst.v30n2.350

volumetric gas throughput, whereas molecular discrimination was comparatively limited because gas transport depended primarily on pressure-driven bulk flow.

In contrast, the 15 nm membrane exhibited lower permeation rates but improved hydrogen-selective transport behaviour. The finer pore structure increased the contribution of Knudsen and transitional transport mechanisms, enhancing gas–wall interactions and improving molecular discrimination between hydrogen and the heavier gases. This behaviour is consistent with the well-established permeability–selectivity trade-off commonly observed in porous membrane systems [43, 51], where reducing pore size generally improves selectivity at the expense of permeance. Comparison with the theoretical Poiseuille-flow analysis further demonstrates that nominal pore diameter alone does not adequately predict gas transport behaviour in practical asymmetric ceramic membranes. Although the membranes differed by a factor of 400 in nominal pore diameter, the experimentally measured hydrogen permeation rates differed by less than a factor of two. This discrepancy confirms that gas transport is governed by the combined effects of pore connectivity, tortuosity, support-layer resistance, effective transport pathways, and overall membrane architecture rather than by nominal pore size alone.

The characterisation results further support this interpretation. SEM observations confirmed that both membranes retained their macroscopic structural integrity following ruthenium impregnation and thermal treatment, while EDX analysis verified the presence of ruthenium within both membrane structures. Although the available SEM resolution and EDX analysis do not permit direct assessment of nanoscale pore coverage or catalyst distribution, the approximately linear permeation behaviour indicates that ruthenium incorporation did not introduce significant transport limitations within the accessible pore network. Contact-angle measurements further demonstrated that Ru impregnation modified the membrane surface properties by altering wettability, indicating changes in the physicochemical environment experienced by permeating gas molecules.

Collectively, these findings indicate that ruthenium functioned primarily as a surface modifier rather than as a structural transport barrier. Under the non-reactive conditions investigated, Ru altered surface characteristics and gas–surface interactions while preserving the dominant transport mechanisms established by the membrane pore architecture.

From a practical membrane design perspective, the 6000 nm membrane is better suited to applications requiring high gas throughput, such as porous support layers and pre-separation stages in membrane-based processing systems. Conversely, the 15 nm membrane is more appropriate for hydrogen-selective separation processes, where improved molecular discrimination is prioritised over maximum permeance.

The present study demonstrates that optimisation of membrane architecture remains the principal strategy for controlling permeation performance, while controlled ruthenium impregnation provides an effective means of modifying membrane surface properties without fundamentally altering the governing gas transport mechanism. These findings provide useful design guidance for the development of Ru-modified ceramic membranes for hydrogen separation and future catalytic membrane reactor applications [13, 48].

* Corresponding to: Muktar M. Ramalan (email: muktarmramalan@gmail.com)
DOI: https://doi.org/10.11113/jamst.v30n2.350

3.8 Surface Wettability and Microstructural Characterisation

Surface wettability and microstructural characterisation were performed to evaluate the effects of ruthenium impregnation and membrane pore architecture on surface properties and their relationship with gas transport behaviour. Dynamic contact angle measurements were used to evaluate the influence of Ru impregnation on membrane wettability, while scanning electron microscopy (SEM) and energy-dispersive X-ray spectroscopy (EDX) were employed to examine membrane morphology, structural features, and elemental composition. The combined characterisation results provide complementary information for interpreting the experimentally observed permeation behaviour and elucidating the relationships between membrane structure, surface modification, and gas transport performance.

3.8.1 Contact Angle Behaviour and Wettability

Figure 6 presents the dynamic contact angle behaviour of the ruthenium-impregnated alumina ceramic membranes with nominal pore sizes of (a) 15 nm and (b) 6000 nm. Both membranes exhibited a progressive decrease in contact angle with time, indicating gradual wetting of the membrane surfaces. However, distinct differences in the wetting behaviour were observed between the two membrane architectures, reflecting the influence of pore structure and surface modification on wettability. However, distinct differences in wetting behaviour were observed between the two membrane structures. The 6000 nm membrane exhibited more rapid droplet spreading and lower contact angles throughout the measurement period, indicating greater apparent wettability and enhanced capillary infiltration through its macroporous structure. In contrast, the 15 nm membrane exhibited higher contact angles and slower wetting kinetics, indicating greater resistance to liquid penetration within the finer pore network.

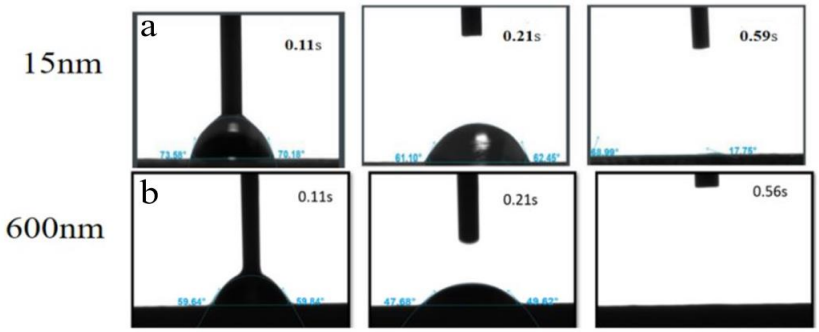

Figure 6. Dynamic contact angle behaviour of ruthenium-impregnated alumina ceramic membranes: (a) 15 nm membrane and (b) 6000 nm membrane

The dynamic contact-angle measurements showed that both Ru-impregnated membranes remained hydrophilic, with initial contact angles below 90°. The 15 nm membrane exhibited a higher initial contact angle of approximately 72° at 0.11 s, whereas the 6000 nm membrane exhibited an initial contact angle of approximately 59°. As the droplets spread over time, the contact angles decreased for both membranes, reaching

* Corresponding to: Muktar M. Ramalan (email: muktarmramalan@gmail.com)
DOI: https://doi.org/10.11113/jamst.v30n2.350

approximately 62° at 0.21 s for the 15 nm membrane and 49° for the 6000 nm membrane before further decreasing as wetting progressed. The faster decrease observed for the 6000 nm membrane indicates more rapid droplet spreading and liquid penetration through its larger pore structure, whereas the finer pore network of the 15 nm membrane delayed liquid infiltration and maintained a larger apparent contact angle throughout the measurement period.

The observed behaviour is consistent with the qualitative interpretation provided by the Young–Wenzel and Cassie–Baxter wetting models introduced in Section 2.6. Surface roughness, pore geometry, and partial air entrapment within the porous structure can influence the apparent contact angle and the rate of droplet spreading on porous ceramic surfaces [52].

These wettability characteristics have important implications for membrane operation. The slower wetting behaviour of the 15 nm membrane suggests greater resistance to liquid penetration, whereas the 6000 nm membrane promotes more rapid liquid infiltration because of its larger and more accessible pore network. These differences in wettability are consistent with the permeation results, where the finer membrane exhibited greater molecular discrimination while the larger-pore membrane favoured higher gas throughput. The contact-angle results indicate that both membrane pore architecture and Ru surface modification influence surface wettability. Although both membranes remained hydrophilic, the 15 nm membrane exhibited lower wettability than the 6000 nm membrane, consistent with its finer pore structure and the gas-transport behaviour observed during the permeation experiments.

3.8.2 SEM and EDX Characterisation

Scanning Electron Microscopy (SEM) and Energy Dispersive X-ray (EDX/EDAX) analyses were performed to examine membrane morphology, structural integrity, elemental composition, and ruthenium distribution within the impregnated alumina membranes. These characterisation techniques provide complementary information for interpreting the experimentally observed permeation and wettability behaviour [53].

Representative SEM micrographs of the ruthenium-impregnated 15 nm and 6000 nm membranes are presented in Figure 7. The combined figure enables direct comparison of the surface morphology of both membrane architectures following ruthenium impregnation, calcination, and reduction. Corresponding EDX spectra and elemental compositions for the two membranes are presented in Figure 8 to verify the elemental composition and confirm successful ruthenium incorporation within the membrane structures.

* Corresponding to: Muktar M. Ramalan (email: muktarmramalan@gmail.com)
DOI: https://doi.org/10.11113/jamst.v30n2.350

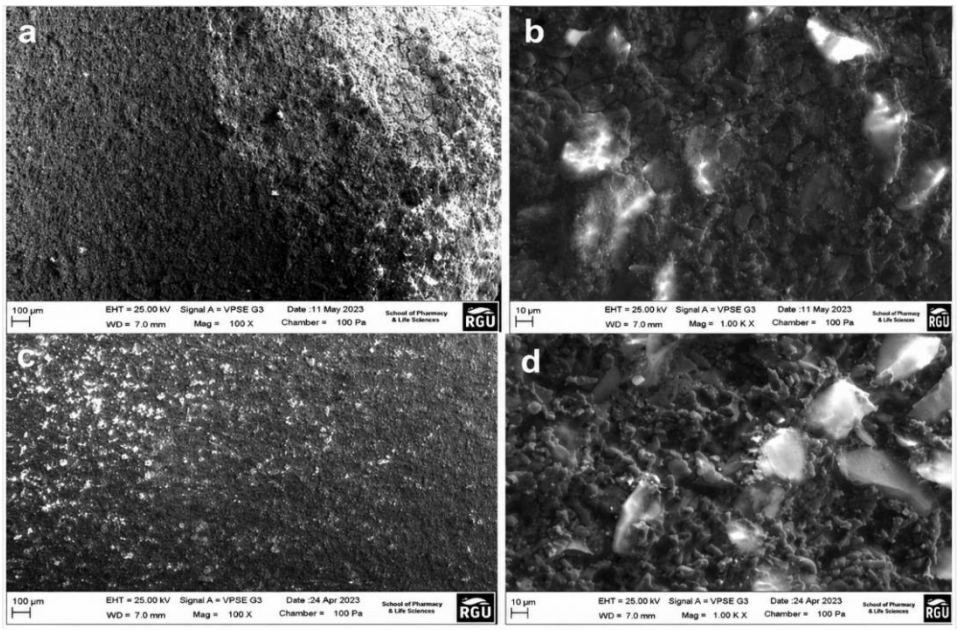

Figure 7. Representative SEM micrographs of ruthenium-impregnated alumina ceramic membranes following calcination and reduction: (a) 15 nm membrane, inner surface (100× magnification); (b) 15 nm membrane, outer surface (1000× magnification); (c) 6000 nm membrane, inner surface (100× magnification); and (d) 6000 nm membrane, outer surface (1000× magnification). The images illustrate the surface morphology and structural integrity of both membranes after ruthenium impregnation and thermal treatment

Element	Weight%	Atomic%
C K	0.10	0.66
O K	10.85	51.28
Al K	2.18	6.12
Si K	1.17	3.15
Ti K	17.87	28.22
V K	0.51	0.75
Fe K	0.52	0.70
Cu K	0.39	0.47
RuL	11.54	8.64
Totals	45.14	

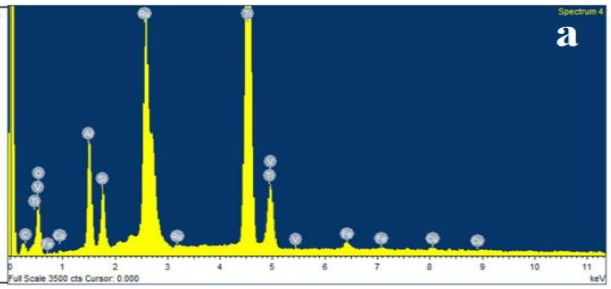

Element	Weight%	Atomic%
O K	37.65	60.89
Al K	6.77	6.49
Si K	8.45	7.79
Ti K	39.70	21.44
Fe K	0.88	0.41
Ru L	11.63	2.98
Totals	105.08	

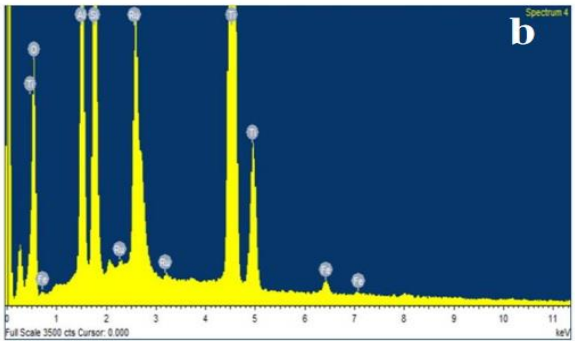

Figure 8. EDX spectrum and elemental composition of ruthenium-impregnated (a)15 nm and (b) 6000nm membrane

* Corresponding to: Muktar M. Ramalan (email: muktarmramalan@gmail.com)
DOI: https://doi.org/10.11113/jamst.v30n2.350

The SEM micrographs indicate that both membranes retained their overall structural integrity following ruthenium impregnation and thermal treatment. No obvious macroscopic structural damage, such as cracking or delamination, was observed. The 6000 nm membrane exhibited a relatively open macroporous morphology consistent with pressure-driven bulk gas transport, whereas the 15 nm membrane displayed a denser surface characteristic of its finer pore structure and selective transport layer.

The SEM magnifications employed (100× and 1000×) were insufficient to resolve individual nanoscale pores, and therefore the presence or absence of partial pore blockage cannot be confirmed directly from the micrographs. Consequently, the SEM observations are interpreted primarily as evidence of preserved membrane morphology and the absence of major structural defects rather than as definitive proof of pore accessibility. Nevertheless, the approximately linear permeation behaviour observed over the investigated pressure range indicates that the accessible gas transport pathways remained functional following Ru impregnation.

The EDX spectra confirmed the presence of oxygen (O), aluminium (Al), titanium (Ti), and silicon (Si), consistent with the alumina–titania ceramic support composition. The dominant oxygen peak reflects the oxide nature of the support matrix, while the aluminium and titanium peaks confirm preservation of the ceramic framework following impregnation and thermal treatment. Distinct ruthenium peaks were detected in both membranes, confirming successful incorporation of Ru from the $RuCl_3$ precursor. Quantitative EDX analysis indicated Ru contents of approximately 11.54 wt.% (8.64 at.%) for the 15 nm membrane and 11.63 wt.% (2.98 at.%) for the 6000 nm membrane, consistent with the elemental compositions presented in Figure 8. Although the Ru weight percentages were similar for both membranes, the difference in atomic percentages reflects the relative elemental composition measured at the analysed locations. Because elemental mapping was not performed, however, the EDX results confirm only the presence of Ru and cannot be used to assess its spatial distribution or uniformity.

Minor traces of carbon and other elements were detected at low concentrations and are attributed to residual contamination or instrumental artefacts commonly encountered during EDX analysis. The absence of significant chlorine peaks indicates effective decomposition of the $RuCl_3$ precursor during the calcination and reduction processes.

The SEM observations confirmed preservation of membrane morphology, whereas the EDX spectra verified successful Ru incorporation into both membrane types. Although the available SEM resolution did not permit direct assessment of nanoscale pore blockage and EDX elemental mapping was not performed to evaluate Ru dispersion, the combined characterisation results, together with the approximately linear gas permeation behaviour observed over the investigated pressure range, indicate that ruthenium modification did not introduce severe structural deterioration or significant obstruction of the accessible gas transport pathways responsible for gas permeation.

4.0 LIMITATIONS AND FUTURE RESEARCH DIRECTIONS

Several limitations of the present study should be acknowledged. The permeation experiments were conducted under single-gas, non-reactive conditions using H_2, He, N_2, CO_2, and air to isolate the influence of pore architecture and ruthenium impregnation on intrinsic transport behaviour. Consequently, competitive adsorption, concentration

* Corresponding to: Muktar M. Ramalan (email: muktarmramalan@gmail.com)
DOI: https://doi.org/10.11113/jamst.v30n2.350

polarisation, and multicomponent diffusion effects encountered in practical hydrogen separation processes were not investigated.

The experiments were performed at a fixed operating temperature of 100 °C over a transmembrane pressure range of 20–300 kPa. Therefore, the influence of broader operating conditions on transport-regime transitions, membrane stability, and long-term permeation performance remains to be established. In addition, only two nominal pore sizes (15 nm and 6000 nm) were investigated, providing a comparison between mesoporous and macroporous transport behaviour but not intermediate pore structures, graded porosity systems, or advanced asymmetric multilayer membrane architectures.

The present work employed a single ruthenium precursor and impregnation protocol. The effects of precursor concentration, impregnation cycles, catalyst loading, reduction conditions, and alternative metallic modifiers were beyond the scope of this study. Furthermore, although SEM and EDX analyses confirmed successful ruthenium incorporation and preservation of membrane morphology, higher-resolution characterisation techniques such as transmission electron microscopy (TEM), X-ray diffraction (XRD), Brunauer–Emmett–Teller (BET) surface-area analysis, X-ray photoelectron spectroscopy (XPS), and EDX elemental mapping would provide more detailed information on Ru particle size, catalyst dispersion, oxidation state, pore characteristics, and metal–support interactions.

Another limitation is that the present investigation focused exclusively on non-reactive gas permeation. Catalytic membrane reactor applications involving simultaneous reaction and separation, including ammonia decomposition, methane steam reforming, and the water–gas shift reaction, were not investigated. Likewise, long-term membrane durability, catalyst deactivation, fouling behaviour, thermal cycling stability, and sealing performance under continuous operation were beyond the scope of the present study.

Future work should therefore include mixed-gas permeation experiments under industrially relevant operating conditions, broader temperature and pressure ranges, optimisation of ruthenium loading and impregnation parameters, investigation of intermediate pore sizes and advanced asymmetric membrane architectures, together with high-resolution structural characterisation and long-term durability studies. Benchmarking the permeation and selectivity performance of Ru-modified ceramic membranes against other ceramic-supported metallic membrane systems would further clarify their practical competitiveness for hydrogen purification applications. Recent studies have also highlighted the potential of advanced ceramic membrane configurations, including asymmetric structures, hollow-fibre membranes, and mixed protonic–electronic conducting membranes, for improving hydrogen separation performance and facilitating industrial implementation [13]. Such investigations would provide a more comprehensive understanding of structure–transport relationships and support the development of Ru-modified ceramic membranes for hydrogen separation and catalytic membrane reactor technologies [13, 48].

Despite these limitations, the present study provides experimental evidence that membrane architecture exerts a greater influence on gas permeation behaviour than nominal pore diameter alone. The findings improve the understanding of gas transport mechanisms in Ru-impregnated ceramic membranes and provide a useful foundation for the future optimisation of hydrogen-selective ceramic membrane systems.

* Corresponding to: Muktar M. Ramalan (email: muktarmramalan@gmail.com)
DOI: https://doi.org/10.11113/jamst.v30n2.350

5.0 CONCLUSIONS

Hydrogen and multi-gas permeation through ruthenium-impregnated α-alumina ceramic membranes with nominal pore sizes of 15 nm and 6000 nm was investigated under non-reactive conditions at 100 °C and transmembrane pressure differences of 20–300 kPa. Permeation rates increased approximately linearly with pressure for all gases, confirming that gas transport was predominantly pressure driven. The 6000 nm membrane exhibited higher permeation rates, whereas the 15 nm membrane provided greater molecular discrimination and improved hydrogen-selective transport behaviour.

Knudsen number analysis showed that transport in the 6000 nm membrane was dominated by viscous flow, while the 15 nm membrane operated within the transitional Knudsen–viscous regime. The experimentally observed permeation order (H_2 > He > N_2 ≈ Air > CO_2) reflected the combined influence of gas molecular properties, pore architecture, and transport mechanisms.

Comparison of the experimental results with classical Poiseuille-flow predictions revealed that the influence of nominal pore diameter was considerably smaller than expected from ideal capillary theory. Although the membranes differed by a factor of 400 in nominal pore diameter, the corresponding hydrogen permeation rates differed by less than a factor of two. This demonstrates that gas transport in practical multilayer ceramic membranes is governed primarily by the combined effects of pore connectivity, tortuosity, support-layer resistance, and effective transport pathways rather than by nominal pore diameter alone.

SEM observations, EDX analysis, contact-angle measurements, and catalyst-loading analysis confirmed successful ruthenium incorporation while preserving membrane morphology and maintaining accessible gas transport pathways. The results further indicate that, under the non-reactive operating conditions investigated, ruthenium primarily acted as a surface modifier by altering membrane surface characteristics, wettability, and gas–surface interactions rather than as a transport barrier or catalytic reaction medium. This surface modification contributed to the observed changes in hydrogen transport behaviour without significantly reducing membrane permeability.

This study demonstrates that membrane architecture and ruthenium-induced surface modification jointly govern gas transport behaviour in ceramic membranes. The work provides experimental evidence that practical permeation behaviour deviates substantially from ideal pore-radius scaling and highlights the importance of considering complete membrane architecture, surface characteristics, and effective transport pathways when designing hydrogen-selective ceramic membranes. These findings improve the understanding of structure–transport relationships in Ru-modified ceramic membranes and provide a foundation for the future optimisation of hydrogen separation systems under mixed-gas and reactive operating conditions.

DECLARATION OF COMPETING INTEREST

The authors declare that they have no known competing financial interests or personal relationships that could have appeared to influence the work reported in this paper.

* Corresponding to: Muktar M. Ramalan (email: muktarmramalan@gmail.com)
DOI: https://doi.org/10.11113/jamst.v30n2.350

ACKNOWLEDGEMENT

The authors would like to express their sincere gratitude to the Centre for Process and Membrane Technology, Robert Gordon University, Aberdeen, United Kingdom, for providing the research facilities and technical support that made this work possible. The authors also sincerely thank Professor Radhakrishna Prabhu and late Professor Edward Gobina for his valuable guidance, encouragement, and technical support throughout the course of this research.

REFERENCES

[1] Imam, J., Singh, P. K., & Shukla, P. (2013). Biohydrogen as biofuel: future prospects and avenues for improvements. In *Biofuel Technologies: Recent Developments* (pp. 301-315). Berlin, Heidelberg: Springer Berlin Heidelberg.

[2] Gunathilake, C., Soliman, I., Panthi, D., Tandler, P., Fatani, O., Ghulamullah, N. A., ... & Jaroniec, M. (2024). A comprehensive review on hydrogen production, storage, and applications. *Chemical Society Reviews*, *53*(22), 10900-10969.

[3] Arutyunov, V. S., & Lisichkin, G. V. (2017). Energy resources of the 21st century: problems and forecasts. Can renewable energy sources replace fossil fuels. *Russian Chemical Reviews*, *86*(8), 777.

[4] Merouani, S., & Dehane, A. (2025). Hydrogen: A pathway to cleaner energy. *Hydrogen Production, Storage and Utilization: Thermochemical, Electrochemical, Sonochemical, Biological and Photocatalytic Processes*, 1.

[5] Staffell, I., Scamman, D., Abad, A. V., Balcombe, P., Dodds, P. E., Ekins, P., ... & Ward, K. R. (2019). The role of hydrogen and fuel cells in the global energy system. *Energy & Environmental Science*, *12*(2), 463-491.

[6] Kumar, R., Chakraborty, P., Singh, P. K., Chakrabortty, S., Tripathy, S. K., Saratale, G. D., ... & Jeon, B. H. (2025). Emerging approaches on biomass and water-based hydrogen production and downstream recovery pathways: a review on recent challenges and prospects. *Reviews in Environmental Science and Bio/Technology*, *24*(4), 957-1018.

[7] Ghorbani, B., Zendehboudi, S., & Saady, N. M. C. (2025). Advancing hybrid cryogenic natural gas systems: a comprehensive review of processes and performance optimization. *Energies*, *18*(6), 1443.

[8] Rey, J. C., Nobre, C., Rijo, B., Longo, A., Brito, P., & Mateos-Pedrero, C. (2026). Recent Advances in Renewable Hydrogen Purification Technologies: A General Review. *Clean Technologies*, *8*(2), 35.

[9] Yang, H., Li, Q., Wu, X., Zhang, K., Li, Z., Zhang, G., ... & Xie, B. (2026). Review of Progress on Application of Functional Ceramic Membranes in Maricultural Wastewater Treatment. *Water*, *18*(11), 1266.

[10] Eren, M. Ş., & Arslanoğlu, H. (2025). α-Alumina (α-Al2O3) ceramic microfiltration membranes in industrial wastewater treatment: Production, design, filtration behavior and performance. *Ceramics International*, *51*(8), 10234-10241.

[11] Jiang, W., Cao, J. P., Zhu, C., Zhao, M., Ni, Z. H., Zhao, X. Y., ... & Bai, H. C. (2022). Catalytic hydrogenation of aromatic ring over ruthenium nanoparticles

* Corresponding to: Muktar M. Ramalan (email: muktarmramalan@gmail.com)
DOI: https://doi.org/10.11113/jamst.v30n2.350

supported on α-Al2O3 at room temperature. *Applied Catalysis B: Environment and Energy*, *307*, 121137.
[12] Romero, N., Axet, M. R., & Philippot, K. (2023). Design of ruthenium nanoparticles for better performance in catalysis. In *Advances in Catalysis* (Vol. 72, pp. 115-158). Academic Press.
[13] Dou, J., Wang, S., & Yao, Z. (2025). Mixed protonic–electronic conducting ceramic membranes for hydrogen separation: A review on recent advances in structure optimization and preparation. *Separation and Purification Technology*, *355*, 129582.
[14] Janiszewska, E., Pietrowski, M., & Zieliński, M. (2026). Catalytic Synergy: Mesoporous Silica and Ruthenium—Structure–Activity Relationships in CO2 Methanation and Toluene Hydrogenation. *Molecules*, *31*(7), 1130.
[15] Cheng, S., Li, X., Huang, X., Ling, Y., Liu, S., & Li, T. (2024). Hydrogen separation via proton conducting ceramic membranes: A review. *International Journal of Hydrogen Energy*, *70*, 654-665.
[16] Aisueni, F., Ramalan, M., Abunumah, O., Ogunlude, P., Orakwe, I., Ogoun, E., ... & Gobina, E. (2023, January). Gas diffusion, transport characteristics and modelling in porous membrane systems with application for polymer electrolyte membrane fuel cells. ICONSAD (International congress on scientific advances).
[17] Alsoy Altinkaya, S. (2024). A review on microfiltration membranes: fabrication, physical morphology, and fouling characterization techniques. *Frontiers in Membrane Science and Technology*, *3*, 1426145.
[18] Chen, Y., Ma, H., & Hsiao, B. S. (2026). Structural Design and Performance Optimization of Proton Exchange Membranes for Water Electrolysis: A Review. *Membranes*, *16*(2), 54.
[19] Tong, J., Zhang, P., Zhuang, F., Zheng, Y., Liu, B., Qiao, X., & Zhu, X. (2024). Mixed-conducting ceramic membrane reactors for hydrogen production. *Reaction Chemistry & Engineering*, *9*(12), 3072-3099.
[20] Cheng, S., Li, X., Huang, X., Ling, Y., Liu, S., & Li, T. (2024). Hydrogen separation via proton conducting ceramic membranes: A review. *International Journal of Hydrogen Energy*, *70*, 654-665.
[21] Maccarrone, D., Italiano, C., Giorgianni, G., Centi, G., Perathoner, S., Vita, A., & Abate, S. (2025). A comprehensive review on hydrogen production via catalytic ammonia decomposition.
[22] Sabouri, R., Ladewig, B. P., & Prasetya, N. (2026). Mixed matrix membranes for hydrogen separation: a comprehensive review and performance analysis. *Journal of Materials Chemistry A*.
[23] Zoudani, E. L., De Saram, P., Feih, S., Vu, H. H., Nguyen, N. T., & Kashaninejad, N. (2026). Micropatterned surfaces with unidirectional wetting properties for liquid transport. *Small Structures*, *7*(2).
[24] Mądry, K., & Nowicki, W. (2021). Wetting between Cassie–Baxter and Wenzel regimes: A cellular model approach. *The European Physical Journal E*, *44*(11), 138.
[25] Yang, J., Zhuang, Z., Wu, N., Zhang, D., Feng, B., Hou, D., & Wang, L. (2025). Gas Transport Mechanisms and Applications Through Graphene-Based Membranes. *Small*, *21*(26), 2502473.

* Corresponding to: Muktar M. Ramalan (email: muktarmramalan@gmail.com)
DOI: https://doi.org/10.11113/jamst.v30n2.350

[26] To, Q. D., Léonard, C., & Lauriat, G. (2015). Free-path distribution and Knudsen-layer modeling for gaseous flows in the transition regime. *Physical Review E*, *91*(2), 023015.
[27] Razavizadeh, S., Rahbari-Sisakht, M., Malekzadeh, A., & Faramarzi, M. (2025). Effect of porous substrate morphology and characteristics on the performance of thin-film composite polyamide reverse osmosis membranes. *Emergent Materials*, *8*(6), 3935-3957.
[28] Reimund, K. K., Sujanani, R., Hernandez, J. M., Gleason, K. L., & Freeman, B. D. (2025). Experimental observation of nonlinear relation between pressure and water flux is consistent with the solution-diffusion model. *Journal of Membrane Science*, 124756.
[29] Gilron, J., & Soffer, A. (2002). Knudsen diffusion in microporous carbon membranes with molecular sieving character. *Journal of membrane science*, *209*(2), 339-352.
[30] Cho, S., Dai, Y., Li, H., & Wang, Y. (2025). Thin Gas Diffusion Layer for Polymer Electrolyte Membrane Fuel Cell: Three-Dimensional Distribution and Performance Loss. *Automotive Innovation*, *8*(3), 556-567.
[31] Ramalan, M. M., Hashim, I., Dauda, M., & Tonye, I. (2026). Knudsen Number Sensitivity to Pressure Drop in Composite Ceramic Membranes. *Journal of Applied Membrane Science & Technology*, *30*(1), 1-22.
[32] Alhathal Alanezi, A., Bassyouni, M., Abdel-Hamid, S. M., Ahmed, H. S., Abdel-Aziz, M. H., Zoromba, M. S., & Elhenawy, Y. (2021). Theoretical investigation of vapor transport mechanism using tubular membrane distillation module. *Membranes*, *11*(8), 560.
[33] Ogunlude, P., Abunomah, O., Hashim, I., Aisueni, F., Ogoun, E., Antwi, S., ... & Gobina, E. (2022). Mass Transfer Characteristics through Alumina Membranes with Different Pores Sizes and Porosity. *International Journal on Engineering, Science and Technology (IJonEST)*, *4*(1), 99-123.
[34] Moghadam, A. A., & Chalaturnyk, R. (2016). Analytical and experimental investigations of gas-flow regimes in shales considering the influence of mean effective stress. *SPE Journal*, *21*(02), 557-572.
[35] de Souza Sá, L. (2026). *Finite-size scaling of transport properties from pore-network models applied to a CT-image of a berea sandstone sample* (Doctoral dissertation, Universidade Federal do Rio de Janeiro).
[36] Anjum, T., Qin, T. H., Olguin, G., Wang, Y., Zhang, D., Kou, X., ... & Ji, G. (2026). Impact of freeze drying on pore size distribution of amorphous silica membranes derived from gas permeation activation energies. *Separation and Purification Technology*, 137736.
[37] Skvortsov, A. T., Dagdug, L., Hilder, E. F., Berezhkovskii, A. M., & Bezrukov, S. M. (2023). Permeability and diffusion resistance of porous membranes: Analytical theory and its numerical test. *The Journal of Chemical Physics*, *158*(5).
[38] Kannan, A. S., Narahari, T. S. B., Bharadhwaj, Y., Mark, A., Sardina, G., Maggiolo, D., ... & Ström, H. (2020). The Knudsen paradox in micro-channel Poiseuille flows with a symmetric particle. *Applied sciences*, *11*(1), 351.
[39] Mou, W., He, G., Zhou, C., Gan, B., Liu, Y., Shi, S., & Xia, M. (2025). Molecular dynamics study on hydrogen permeation behavior and mechanism in polyethylene type IV hydrogen storage cylinder liner. *The Journal of Chemical Physics*, *162*(23).

* Corresponding to: Muktar M. Ramalan (email: muktarmramalan@gmail.com)
DOI: https://doi.org/10.11113/jamst.v30n2.350

[40] Lasseuguette, E., Malpass-Evans, R., Carta, M., McKeown, N. B., & Ferrari, M. C. (2018). Temperature and pressure dependence of gas permeation in a microporous Tröger's base polymer. *Membranes*, *8*(4), 132.
[41] Li, A., Liu, S., Li, R., Chen, J., Chen, C., Zhang, J., ... & Wang, J. (2025). Molecule transport behaviors in ultrathin and porous membranes: The role of pore size. *Journal of Membrane Science*, *721*, 123835.
[42] Jiang, Y., Pi, Y., Wang, R., Liang, C., & Jiao, F. (2026). Breaking the permeability–selectivity trade-off in separation membranes with vertically aligned MXene nanosheets. *Coordination Chemistry Reviews*, *564*, 218035.
[43] Rahman, M. H. (2026). Temperature-Driven Transition from Knudsen Diffusion to Viscous Flow in a Macroporous Ceramic Membrane. *Ceramics*, *9*(5), 46.
[44] Sibiryakov, B., Leite, L. W. B., & Sibiriakov, E. (2021). Porosity, specific surface area and permeability in porous media. *Journal of Applied Geophysics*, *186*, 104261.
[45] Wan, Q., Hu, X., Yu, T., Guo, P., Wang, J., Shi, H., & Chen, S. (2024). Wetting state transition of laser direct writing aluminum surface based on coupling effect of micro/nanoscale characteristics. *Langmuir*, *40*(29), 15196-15204.
[46] Iqbal, M. H., Quetzeri-Santiago, M. A., Castrejón-Pita, A. A., & Castrejón-Pita, J. R. (2025). Droplet impact onto textiles: Wetting, spreading, and lamella-controlled splashing. *Journal of Colloid and Interface Science*, 139385.
[47] Konstantinidis, K., Göhl, J., Mark, A., Yan, X., Miljkovic, N., & Sasic, S. (2025). The role of surface microstructures in particle-droplet coalescence and jumping from superhydrophobic surfaces. *Surfaces and Interfaces*, *64*, 106333.
[48] Xie, S., Hou, C., Chen, X., Peng, Y., Zhang, X., Zhang, C., ... & Liu, S. (2025). Wetting state transition of porous hydrophobic membrane in direct-contact membrane distillation. *Separation and Purification Technology*, *372*, 133367.
[49] Zhou, J., Peng, T., Jiang, L., Chen, G., Xu, L., & Li, J. (2026). Transport-oriented ordered architectures in membrane electrode assemblies for high-performance proton exchange membrane fuel cells. *Sustainable Energy & Fuels*.
[50] Wesley, G., Swetlech, E., Velasco, C., Williams, A., Larsen, K., Antony Jose, S., & Menezes, P. L. (2026). Catalytic Materials for Hydrogen Generation: Design, Properties, and Applications in Sustainable Energy Systems. *Processes*, *14*(6), 957.
[51] Yu, S., Chen, Y., Qiao, Z., & Hou, J. (2026). Processable microporous membranes: emerging platforms for separation technologies. *Chemical Society Reviews*, *55*(4), 2229-2264.
[52] Anil, A., & ES, H. S. (2026). Engineering Hydrophobicity in Cement-Based Materials: A Critical Review of Advances in Hydrophobic Cement Composites. *Iranian Journal of Science and Technology, Transactions of Civil Engineering*, 1-35.
[53] Shekh, M. I., Masum, M. S. I., Rafi, R. H., Murshed, I., Sayem, S. S., Akash, A. A., ... & Mahmud, S. (2026). Adsorbent-modified membranes for selective contaminant removal-surface functionalization strategies and performance enhancement. *Journal of Materials Science*, 1-38.

* Corresponding to: Muktar M. Ramalan (email: muktarmramalan@gmail.com)
DOI: https://doi.org/10.11113/jamst.v30n2.350